Gas-phase metallicity of 27 galaxies at intermediate redshift[*,**]
(Research Note)

L. Morelli[1,2], V. Calvi[1,3], A. Cardullo[1], A. Pizzella[1,2], E. M. Corsini[1,2], and E. Dalla Bontà[1,2]

[1] Dipartimento di Fisica e Astronomia "G. Galilei", Università di Padova, vicolo dell'Osservatorio 3, 35122 Padova, Italy
   e-mail: lorenzo.morelli@unipd.it
[2] INAF – Osservatorio Astronomico di Padova, vicolo dell'Osservatorio 2, 35122 Padova, Italy
[3] Space Telescope Science Institute, 3700 San Martin Drive, Baltimore, MD 21218, USA

ABSTRACT

Aims. The purpose of this work is to make available new gas-phase oxygen abundance measurements for a serendipitous sample of 27 galaxies with redshifts $0.35 \leq z \leq 0.52$.
Methods. We measured the equivalent widths of the [O II]$\lambda 3727$, Hβ, and [O III]$\lambda\lambda 4959, 5007$ emission lines observed in the galaxy spectra obtained with the Visible Multi-Object Spectrograph mounted at the Very Large Telescope. For each galaxy, we derived the metallicity-sensitive emission-line ratio R_{23}, ionization-sensitive emission-line ratio O_{32}, and gas-phase oxygen abundance $12 + \log(O/H)$.
Results. The values of the gas-phase oxygen abundance $12 + \log(O/H)$ that we obtained for all the sample galaxies are consistent with previous findings for galaxies at intermediate redshift.

Key words. galaxies: distances and redshifts – galaxies: evolution – galaxies: formation – galaxies: fundamental parameters – galaxies: ISM

1. Introduction

The gas-phase metallicity is one of the most important observational diagnostics of the current evolutionary state of galaxies. Accurate gas-phase metallicity measurements are crucial for investigating the interplay between fundamental processes, such as star formation, gas accretion, gas flows, and supernova-driven winds occurring during the life of galaxies (e.g., Moustakas et al. 2011; Cresci et al. 2012; Sommariva et al. 2012).

The galaxy gas-phase metallicity correlates with many properties, such as the star formation rate (Mannucci et al. 2010; Lara-López et al. 2010), morphological type (Edmunds & Pagel 1984), surface mass density (Ryder 1995; Garnett et al. 1997), and maximum rotation velocity (Dalcanton 2007). In particular, the metallicity Z most strongly correlates with the mass M and B-band luminosity L of the galaxy (McClure & van den Bergh 1968; Skillman et al. 1989; Richer & McCall 1995). Adopting the Sloan Digital Sky Survey (SDSS, Abazajian et al. 2009), Tremonti et al. (2004) and Gallazzi et al. (2005) derived the $M - Z$ and $L - Z$ relations in the local Universe for a large sample of galaxies on the basis of the gas-phase metallicity. These relations are very tight with a scatter of less than 0.1 dex and show that the more luminous galaxies have higher gas metallicities than their fainter counterparts, which has a great impact on the theoretical models of galaxy formation.

Another crucial piece of information to help us to understand the assembly history of galaxies comes from the study of the evolution of the $M - Z$ and $L - Z$ relations across cosmic time.

This topic has been investigated by measuring the gas-phase metallicity of galaxies as a function of redshift up to $z \sim 3.5$. While these relations show clear evidence of galactic evolution at high z, because at a given mass higher-z galaxies have lower metallicities (Shapley et al. 2004; Erb et al. 2006; Maiolino et al. 2008; Mannucci et al. 2009; Rodrigues et al. 2012), at intermediate redshift ($z < 1$) it is still debated whether there has been any evolution. Carollo & Lilly (2001) and Kobulnicky & Kewley (2004) found that the $L - Z$ relation at intermediate redshift is consistent with the local one. In contrast, Maier et al. (2005), Savaglio et al. (2005), and Zahid et al. (2011) measured lower metallicities for intermediate-redshift objects than for local galaxies, supporting a scenario in which the $L - Z$ and $M - Z$ relations also evolve over the range of redshifts between 0.5 and 1.

In this research note, we therefore present new measurements of the equivalent widths for the [O II]$\lambda 3727$, Hβ, [O III]$\lambda 4959$, and [O III]$\lambda 5007$ emission-lines and present our derived metallicity-sensitive emission lines ratios R_{23}, ionization-sensitive emission-lines ratios O_{32}, and gas-phase oxygen abundances $12 + \log(O/H)$ for 27 intermediate-redshift ($0.35 \leq z \leq 0.52$) galaxies. The data that we analised for all the sample galaxies are available from the SDSS archive, hence our measurements are a valuable supplementary resource for the astronomical community.

2. Observations and data reduction

As often happens, the data acquired for a particular aim can potentially contain information useful for different purposes. For this work, we used observations carried out in 2006 at the Very Large Telescope (VLT) of the European Southern Observatory (ESO) at Paranal Observatory using the VIsible Multi-Object Spectrograph (VIMOS). The main goal of these observations

---

[*] Based on observations made with ESO Telescopes at the La Silla-Paranal Observatory under programmes 075.B-0794 and 077.B-0767.
[**] Tables 1 and 3 are available in electronic form at http://www.aanda.org

was to find satellites in the region of $\sim 500 \times 500$ kpc^2 surrounding seven nearby isolated spiral galaxies (Yegorova et al. 2011).

VIMOS was used in Multi Object Spectroscopy (MOS) mode with the grism "HR orange" and the order sorting-filter GG435. The grism is characterized by a reciprocal dispersion of 0.6 Å pixel^{-1} and a spectral resolution of $R = 2150$ for the adopted 1″0 slit. In the high-resolution configuration that we used for the observations, the spectral range strongly depends on the position of the slit in the field of view varying from 4550–6950 Å to 6000–8400 Å. The full dataset includes MOS observations of 7 different fields for a total exposure time of ~ 20 h. This granted a typical exposure time of ~ 3 h for each target field. Each of the four quadrants of VIMOS observed ~ 50 objects so as to have ~ 200 galaxies within each field of view of 16″0 × 18″0.

The observed sample consists of 1450 objects with SDSS r-band magnitudes ranging from 17 mag to 24 mag and a modal value of 22 mag. As expected, only a small fraction of the target galaxies were found to be satellites. We focused on the remaining 1347 background and foreground objects to measure their gas-phase metallicities. Their spectra were bias-subtracted, corrected for flat-field effect, cleaned of cosmic rays, and wavelength-calibrated by means of the ESO VIMOS data reduction pipeline. A more detailed description of the data reduction is reported in Yegorova et al. (2011).

3. Sample selection

To estimate the gas-phase metallicity, it is necessary to know the electron temperature provided by the comparison between auroral and nebular emission lines (Osterbrock 1989). However, since auroral lines are generally weak, it is difficult to observe them in distant galaxies. To overcome this issue, empirical relations between the intensity of the nebular lines and metallicity have been used to derive the gas-phase metallicity. The most widely used metallicity indicator is the R_{23} emission lines ratio parameter (Pagel et al. 1979) defined as

$$R_{23} = \frac{[\text{O II}]\lambda 3727 + [\text{O III}]\lambda 4959 + [\text{O III}]\lambda 5007}{\text{H}\beta}. \quad (1)$$

For our analysed dataset the signal-to-noise ratio (S/N) of the spectra allowed us to measure redshifts for only 571 objects out of the observed 1347 galaxies. We fitted all the available emission lines with Gaussians. The [O II]$\lambda 3727$ doublet was modelled with two Gaussians of the same full width at half maximum. The galaxy redshift was computed as the average of the redshifts derived from the central wavelengths of the measured emission lines.

We detected 177 galaxies in the redshift range between 0.35 and 0.6. However, most of their spectra did not map all the [O II]$\lambda 3727$, Hβ, and [O III]$\lambda\lambda 4959, 5007$ emission-lines we needed to compute the metallicity-sensitive emission-lines ratio R_{23}, ionization-sensitive emission lines ratio O_{32}, and gas-phase oxygen abundance $12 + \log(\text{O/H})$, because of their actual position in the VIMOS field of view. All the relevant emission lines fall in the observed spectral range only for 27 objects, which represent our final sample of galaxies. They are listed in Table 1 and the distribution of their measured redshifts is shown in Fig. 1.

4. Data analysis and gas-phase metallicity

The apparent g-band Petrosian magnitudes of the sample galaxies range between 24.9 and 20.8 mag, as they were derived from
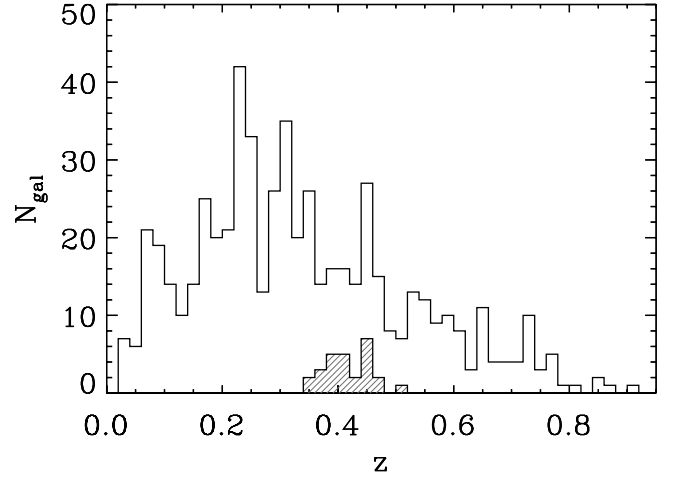

Fig. 1. Distribution of redshifts for the 571 galaxies with measured emission lines. The shaded histogram shows the distribution of the serendipitous sample of 27 objects presented in this work.

the SDSS DR7. Since the S/N of the spectra was too low to derive the radial distribution of the gas metallicity, we rebinned the spectra along the spatial direction to obtain a $S/N \geq 15$ per resolution element.

Since no spectrophotometric standard star had been observed, the galaxy spectra were not flux-calibrated. Furthermore, the observed spectral range does not include the Hα emission line and thus a reliable reddening estimation was not possible. For the above reasons, we followed the approach suggested by Kobulnicky & Phillips (2003) by replacing the flux of the emission-lines with their equivalent width when measuring the gas-phase metallicity. This method does not need flux-calibrated spectra and has the further advantage of being insensitive to reddening. In addition, Kobulnicky & Phillips (2003) verified that the error associated with the use of the emission-line equivalent widths is smaller than both the typical error in the flux measurement and systematic error in the R_{23} and $12 + \log(\text{O/H})$ calibrations. Thus, we measured the equivalent widths of the [O II]$\lambda 3727$, Hβ, and [O III]$\lambda\lambda 4959, 5007$ emission lines in the rest frame spectra. For each emission line, we considered a central bandpass covering the feature of interest and two adjacent bandpasses, at the red and blue side, tracing the local continuum. The continuum level underlying the emission line was estimated by interpolating a straight line in the continuum bandpasses. The bandpasses were defined following Fisher et al. (1998) for [O II]$\lambda 3727$ and Gonzalez (1993) for Hβ, [O III]$\lambda 4959$, and [O III]$\lambda 5007$. The bandpasses are listed in Table 2 and shown in Fig. 2. The errors associated with the measured equivalent widths were derived from photon statistics and CCD read-out noise, and calibrated by means of Monte Carlo simulations.

A well-known problem in measuring the equivalent width of the Hβ emission line in galaxies is the contamination by the Hβ absorption line. We tried to address this issue by using GANDALF (Gas AND Absorption Line fitting; Sarzi et al. 2006) to fit the galaxy spectra with synthetic stellar population models, as done by Morelli et al. (2008, 2012). A linear combination of template stellar spectra from the ELODIE library by Prugniel & Soubiran (2001) was convolved with the line-of-sight velocity distribution and fitted to the observed galaxy spectrum by χ^2 minimization in pixel space. However, the low S/N of the stellar continuum of the galaxy spectra prevented us from deriving a reliable combination of stellar templates to fit the galaxy

Table 2. Definition of the bandpasses for the emission lines.

Emission line	Central bandpass [Å]	Continuum bandpasses [Å]	Reference
(1)	(2)	(3)	(4)
[O II]λ3727	3716.30−3738.30	3696.30−3716.30	1
		3738.30−3758.30	1
Hβ	4851.32−4871.32	4815.00−4845.00	2
		4880.00−4930.00	2
[O III]λ4959	4948.92−4968.92	4885.00−4935.00	2
		5030.00−5070.00	2
[O III]λ5007	4996.85−5016.85	4885.00−4935.00	2
		5030.00−5070.00	2

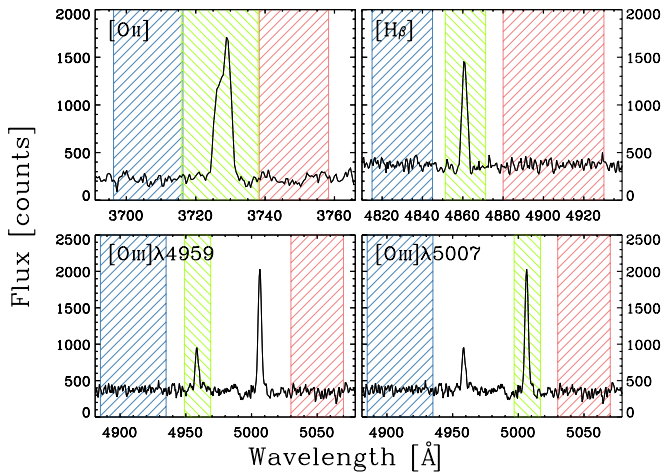**References.** 1 = Fisher et al. (1998); 2 = Gonzalez (1993).

Fig. 2. Central (green dashed region) and continuum bandpasses (blue and red dashed regions) adopted for measuring the equivalent widths of the [O II]λ3727 (*top left panel*), Hβ (*top right panel*), [O III]λ4959 (*bottom left panel*), and [O III]λ5007 (*bottom right panel*) emission lines.

stellar component. Therefore, to account for the Hβ absorption-line contamination we followed Kobulnicky & Kewley (2004) by applying a correction of 2 Å (Kobulnicky & Phillips 2003) to the measured equivalent width of the Hβ emission line used to derive the gas-phase metallicity.

All the equivalent widths measured for the galaxies in our sample are reported in Table 1. They were used to compute the metallicity-sensitive emission-line ratio R_{23}, as well as the emission-line ratio O_{32} defined by Kobulnicky & Kewley (2004) as

$$O_{32} = \frac{[\text{O III}]\lambda4959 + [\text{O III}]\lambda5007}{[\text{O II}]\lambda3727}, \qquad (2)$$

which is mostly sensitive to the ionization (Nagao et al. 2006). All the values of $\log(R_{23})$ and $\log(O_{32})$ are listed in Table 3.

For the sample galaxies, we could not derive the [N II]λ6583/Hα ratio, thus it was impossible to break the R_{23} degeneracy. Following Kobulnicky & Zaritsky (1999) and Kobulnicky et al. (2003), we assumed that all the galaxies lie in the upper branch (12 + log(O/H) $\geq$ 8.4) of the R_{23}-O/H relation. We then checked the consistency of this assumption by adopting the [O III]/[O II] diagnostic lines ratio as proposed by Maiolino et al. (2008). As done by Kobulnicky & Kewley (2004), we derived the gas-phase oxygen abundance by averaging the values obtained from the calibrations for the upper
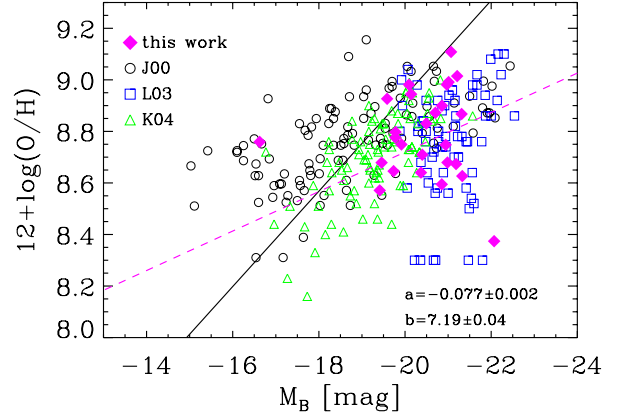

Fig. 3. Plot of our data (solid diamonds) on the $L − Z$ plane. Open squares represent the galaxies in the redshift range $0.47 < z < 0.92$ from the Canada-France Redshift Survey (Lilly et al. 2003), open triangles mark the galaxies with $0.3 < z < 0.6$ from the GOODS-North Field (Kobulnicky & Kewley 2004), and open circles refer to the local galaxies of the Nearby Field Galaxy Sample (Jansen et al. 2000). The solid line indicates the $L − Z$ relation obtained by Tremonti et al. (2004) for local galaxies. The magenta dashed line represents the linear fit (12 + log(O/H)= aM_B + b) through our data points except for J154925.24-003717.8 and J003806.59+000421.9.

branch given in McGaugh (1991) and Kewley & Dopita (2002). The values of 12 + log(O/H) and their uncertainties, owing to the statistical measurement errors in the equivalent widths, are listed in Table 3. The systematic errors due to the uncertainties in the photoionization models (0.2−0.5 dex; Kennicutt et al. 2003; Garnett et al. 2004) were not taken into account.

In Fig. 3, we plot the oxygen abundance as a function of the absolute magnitude in the B-band M_B for the sample galaxies. We derived M_B from the rest-frame g-band Petrosian magnitude given in the SDSS DR7, using the transformation $B = g + 0.327(g − r) + 0.216$ (Chonis & Gaskell 2008). The resulting values are given in Table 3. We also plotted the data for local (Nearby Field Galaxy Sample, Jansen et al. 2000; SDSS, Tremonti et al. 2004) and intermediate-redshift galaxies (Canada-France Redshift Survey, Lilly et al. 2003; GOODS-North Field, Kobulnicky & Kewley 2004).

The dashed magenta line in Fig. 3 represents the linear fit to the sample galaxies. J154925.24-003717.8 and J003806.59+000421.9 are two outliers in the $L − Z$ distribution. The most prominent outlier is the faintest galaxy of the sample, for which the assumption of an upper R_{23}-O/H branch could be incorrect (Skillman et al. 1989). Adopting the calibration of Kewley & Dopita (2002) for the lower branch, we obtained a value of 12 + log(O/H) = 8.14. However only the measurement of the [N II]λ6583 /Hα ratio could firmly help us to discriminate between the two branches. The second outlier has an extremely low value of the gas-phase metallicity. This is probably due to an underestimation of the Hβ absorption-line correction. The slope and zero-point of the fitted $L − Z$ relation to our data points (calculated after excluding the two outliers) are consistent within the errors with the slope and zero-point obtained by Kobulnicky & Kewley (2004) for their sample of galaxies in the redshift range 0.2−0.4. This was expected since 23 of our 27 galaxies have a redshift in the range 0.35−0.45, and confirms their findings of an evolution in the $L − Z$ relation since intermediate redshift.

Finally, we estimated the star formation rate (SFR) of the sample galaxies from their B-band absolute magnitudes and Hβ equivalent widths according to the relations of

Kennicutt et al. (2003) and Kobulnicky & Kewley (2004)

$$SFR \left(M_\odot \, \mathrm{yr}^{-1} \right) = \frac{2.8 \times 5.49 \times 10^{31} \times 2.5^{M_B} EW_{H\beta}}{1.26 \times 10^{41}}. \qquad (3)$$

The derived SFRs are reported in Table 3.

5. Conclusion

Our original purpose was to explore the evolution of the $L - Z$ relation of Tremonti et al. (2004) to the intermediate-redshift range using a large number of background galaxies in very deep VIMOS data. After combining all the constraints needed to perform our analysis, the number of objects dramatically decreased from 1347 to 27, preventing us from being able to draw any conclusion about the possible evolution of the $L - Z$ relation with redshift. Here, we have reported the measured equivalent widths of the [O II]λ3727, Hβ, [O III]λ4959, and [O III]λ5007 emission lines, the values of the metallicity-sensitive emission-line ratio R_{23}, the ionization-sensitive emission-line ratio O_{32}, and the gas-phase oxygen abundances $12 + \log(\mathrm{O/H})$ derived for the serendipitous sample of 27 galaxies with the aim of making them available to the community. Our measurements are consistent with those of Lilly et al. (2003) and Kobulnicky & Kewley (2004) for galaxies in the redshift range $0.3 < z < 1.0$.

References

Abazajian, K. N., Adelman-McCarthy, J. K., Agüeros, M. A., et al. 2009, ApJS, 182, 543
Carollo, C. M., & Lilly, S. J. 2001, ApJ, 548, L153
Chonis, T. S., & Gaskell, C. M. 2008, AJ, 135, 264
Cresci, G., Mannucci, F., Sommariva, V., et al. 2012, MNRAS, 421, 262
Dalcanton, J. J. 2007, ApJ, 658, 941
Edmunds, M. G., & Pagel, B. E. J. 1984, MNRAS, 211, 507
Erb, D. K., Shapley, A. E., Pettini, M., et al. 2006, ApJ, 644, 813
Fisher, D., Fabricant, D., Franx, M., & van Dokkum, P. 1998, ApJ, 498, 195
Gallazzi, A., Charlot, S., Brinchmann, J., White, S. D. M., & Tremonti, C. A. 2005, MNRAS, 362, 41
Garnett, D. R., Shields, G. A., Skillman, E. D., Sagan, S. P., & Dufour, R. J. 1997, ApJ, 489, 63
Garnett, D. R., Kennicutt, Jr., R. C., & Bresolin, F. 2004, ApJ, 607, L21
Gonzalez, J. J. 1993, Ph.D. Thesis, Univ. California, Santa Cruz
Jansen, R. A., Fabricant, D., Franx, M., & Caldwell, N. 2000, ApJS, 126, 331
Kennicutt, Jr., R. C., Bresolin, F., & Garnett, D. R. 2003, ApJ, 591, 801
Kewley, L. J., & Dopita, M. A. 2002, ApJS, 142, 35
Kobulnicky, H. A., & Kewley, L. J. 2004, ApJ, 617, 240
Kobulnicky, H. A., & Phillips, A. C. 2003, ApJ, 599, 1031
Kobulnicky, H. A., & Zaritsky, D. 1999, ApJ, 511, 118
Kobulnicky, H. A., Willmer, C. N. A., Phillips, A. C., et al. 2003, ApJ, 599, 1006
Lara-López, M. A., Bongiovanni, A., Cepa, J., et al. 2010, A&A, 519, A31
Lilly, S. J., Carollo, C. M., & Stockton, A. N. 2003, ApJ, 597, 730
Maier, C., Lilly, S. J., Carollo, C. M., Stockton, A., & Brodwin, M. 2005, ApJ, 634, 849
Maiolino, R., Nagao, T., Grazian, A., et al. 2008, A&A, 488, 463
Mannucci, F., Cresci, G., Maiolino, R., et al. 2009, MNRAS, 398, 1915
Mannucci, F., Cresci, G., Maiolino, R., Marconi, A., & Gnerucci, A. 2010, MNRAS, 408, 2115
McClure, R. D., & van den Bergh, S. 1968, AJ, 73, 1008
McGaugh, S. S. 1991, ApJ, 380, 140
Morelli, L., Pompei, E., Pizzella, A., et al. 2008, MNRAS, 389, 341
Morelli, L., Corsini, E. M., Pizzella, A., et al. 2012, MNRAS, 423, 962
Moustakas, J., Zaritsky, D., Brown, M., et al. 2011, ApJ, submitted [arXiv:1112.3300]
Nagao, T., Maiolino, R., & Marconi, A. 2006, A&A, 459, 85
Osterbrock. 1989, Astrophysics of Gaseous Nebulae and Active Galactic Nuclei (Mill Valley: University Science Books)
Pagel, B. E. J., Edmunds, M. G., Blackwell, D. E., Chun, M. S., & Smith, G. 1979, MNRAS, 189, 95
Prugniel, P., & Soubiran, C. 2001, A&A, 369, 1048
Richer, M. G., & McCall, M. L. 1995, ApJ, 445, 642
Rodrigues, M., Puech, M., Hammer, F., Rothberg, B., & Flores, H. 2012, MNRAS, 421, 2888
Ryder, S. D. 1995, ApJ, 444, 610
Sarzi, M., Falcón-Barroso, J., Davies, R. L., et al. 2006, MNRAS, 366, 1151
Savaglio, S., Glazebrook, K., Le Borgne, D., et al. 2005, ApJ, 635, 260
Shapley, A. E., Erb, D. K., Pettini, M., Steidel, C. C., & Adelberger, K. L. 2004, ApJ, 612, 108
Skillman, E. D., Kennicutt, R. C., & Hodge, P. W. 1989, ApJ, 347, 875
Sommariva, V., Mannucci, F., Cresci, G., et al. 2012, A&A, 539, A136
Tremonti, C. A., Heckman, T. M., Kauffmann, G., et al. 2004, ApJ, 613, 898
Yegorova, I. A., Pizzella, A., & Salucci, P. 2011, A&A, 532, A105
Zahid, H. J., Kewley, L. J., & Bresolin, F. 2011, ApJ, 730, 137

Table 1. Measured properties of the sample galaxies.

Galaxy name SDSS (1)	[O ɪɪ]λ3727 [Å] (2)	Hβ [Å] (3)	[O ɪɪɪ]λ4959 [Å] (4)	[O ɪɪɪ]λ5007 [Å] (5)	z (6)
J003845.31+000006.8	2.95 ± 0.45	1.43 ± 0.49	10.01 ± 0.66	26.35 ± 0.45	0.451
J003838.68+000225.1	92.41 ± 0.68	22.22 ± 0.31	15.58 ± 0.72	46.25 ± 0.69	0.408
J003806.59+000421.9	208.77 ± 7.16	15.75 ± 1.07	9.98 ± 2.50	39.45 ± 1.30	0.474
J134235.94+014424.1	3.89 ± 0.41	3.78 ± 0.54	1.61 ± 0.46	9.17 ± 0.68	0.411
J134229.37+015244.5	58.21 ± 0.58	20.63 ± 0.48	17.33 ± 0.77	43.93 ± 0.69	0.372
J134156.84+014241.0	6.09 ± 0.47	4.79 ± 1.57	3.74 ± 0.87	13.11 ± 0.82	0.390
J145221.51+043448.8	23.01 ± 0.55	9.14 ± 0.15	−0.12 ± 0.45	5.17 ± 0.35	0.450
J145150.75+044111.6	7.09 ± 0.37	3.23 ± 0.83	2.74 ± 0.78	2.76 ± 0.40	0.425
J145147.24+043654.2	30.29 ± 1.13	6.28 ± 1.68	4.61 ± 1.35	6.12 ± 1.17	0.517
J145156.20+043321.7	7.92 ± 0.61	2.16 ± 0.12	4.13 ± 0.25	14.93 ± 0.32	0.416
J145147.77+043244.5	11.84 ± 0.61	1.03 ± 0.79	2.70 ± 0.75	4.18 ± 0.81	0.414
J145149.20+043501.6	14.03 ± 1.09	2.90 ± 0.50	1.57 ± 0.84	8.16 ± 0.67	0.443
J152638.18+034353.8	15.42 ± 0.36	9.75 ± 0.46	4.80 ± 0.79	15.49 ± 0.51	0.407
J152630.18+035110.8	19.58 ± 0.57	5.93 ± 0.45	3.27 ± 1.01	4.39 ± 0.60	0.458
J152559.83+035249.3	18.67 ± 0.45	3.24 ± 0.59	3.30 ± 0.67	8.50 ± 0.56	0.475
J152606.03+034530.7	34.36 ± 0.54	9.08 ± 0.65	6.12 ± 0.44	30.29 ± 0.36	0.386
J154933.50-004255.0	39.71 ± 0.57	14.98 ± 0.27	14.95 ± 0.68	51.32 ± 0.46	0.358
J154931.48-003406.1	45.92 ± 0.59	21.36 ± 0.62	28.59 ± 0.42	107.08 ± 0.36	0.386
J154925.24-003717.8	18.21 ± 0.45	4.76 ± 0.63	2.99 ± 0.32	13.41 ± 0.32	0.386
J154914.49-004010.2	30.77 ± 0.65	9.05 ± 0.43	4.52 ± 0.89	11.21 ± 0.51	0.441
J154925.12-003645.4	18.54 ± 0.34	5.50 ± 0.45	1.90 ± 0.19	7.83 ± 0.37	0.445
J222013.98-074355.8	6.41 ± 0.47	2.06 ± 0.20	1.00 ± 0.32	1.29 ± 0.24	0.399
J222014.86-073333.7	23.12 ± 1.01	7.10 ± 0.88	1.51 ± 1.52	10.07 ± 1.57	0.440
J221934.90-073825.9	7.73 ± 0.89	3.44 ± 0.29	8.27 ± 0.42	26.36 ± 0.35	0.433
J221941.85-074703.8	14.91 ± 0.58	2.52 ± 0.57	2.88 ± 0.52	2.38 ± 0.34	0.369
J221939.28-074744.5	1.72 ± 0.37	0.88 ± 0.14	0.31 ± 0.34	0.62 ± 0.32	0.351
J221941.90-074825.7	29.10 ± 0.60	7.12 ± 0.49	6.26 ± 0.63	15.38 ± 0.21	0.375

Notes. Column (1): SDSS name of the galaxy. Columns (2−5): equivalent widths of the [O ɪɪ]λ3727, Hβ, [O ɪɪɪ]λ4959, and [O ɪɪɪ]λ5007 emission lines, respectively. Column (6): measured redshift.

Table 3. Derived properties of the sample galaxies.

Galaxy name SDSS (1)	M_B [mag] (2)	$\log(R_{23})$ (3)	$\log(O_{32})$ (4)	$12 + \log(O/H)$ (5)	SFR [$M_\odot\,yr^{-1}$] (6)
J003845.31+000006.8	−22.06	$1.06^{+0.01}_{-0.01}$	$1.09^{+0.06}_{-0.07}$	8.37 ± 0.03	1.05
J003838.68+000225.1	−21.32	$0.80^{+0.02}_{-0.02}$	$-0.17^{+0.01}_{-0.02}$	8.63 ± 0.02	8.33
J003806.59+000421.9	−21.46	$1.16^{+0.01}_{-0.01}$	$-0.62^{+0.02}_{-0.03}$	7.72 ± 0.06	6.71
J134235.94+014424.1	−20.09	$0.40^{+0.02}_{-0.02}$	$0.44^{+0.05}_{-0.06}$	8.98 ± 0.02	0.45
J134229.37+015244.5	−19.91	$0.72^{+0.01}_{-0.01}$	$0.02^{+0.01}_{-0.03}$	8.75 ± 0.01	2.11
J134156.84+014241.0	−19.58	$0.53^{+0.02}_{-0.02}$	$0.44^{+0.04}_{-0.04}$	8.93 ± 0.02	0.36
J145221.51+043448.8	−20.97	$0.40^{+0.01}_{-0.01}$	$-0.65^{+0.04}_{-0.05}$	8.98 ± 0.03	2.46
J145150.75+044111.6	−21.01	$0.38^{+0.03}_{-0.03}$	$-0.10^{+0.06}_{-0.08}$	8.99 ± 0.04	0.90
J145147.24+043654.2	−20.94	$0.69^{+0.02}_{-0.02}$	$-0.45^{+0.06}_{-0.08}$	8.75 ± 0.06	1.65
J145156.20+043321.7	−21.18	$0.81^{+0.01}_{-0.01}$	$0.38^{+0.03}_{-0.03}$	8.67 ± 0.02	0.70
J145147.77+043244.5	−20.36	$0.79^{+0.02}_{-0.03}$	$-0.23^{+0.06}_{-0.08}$	8.64 ± 0.07	0.16
J145149.20+043501.6	−19.77	$0.68^{+0.02}_{-0.02}$	$-0.15^{+0.05}_{-0.06}$	8.78 ± 0.05	0.26
J152638.18+034353.8	−20.14	$0.48^{+0.01}_{-0.01}$	$0.11^{+0.02}_{-0.02}$	8.94 ± 0.01	1.23
J152630.18+035110.8	−20.85	$0.53^{+0.02}_{-0.02}$	$-0.40^{+0.06}_{-0.07}$	8.90 ± 0.04	1.44
J152559.83+035249.3	−20.98	$0.76^{+0.01}_{-0.01}$	$-0.19^{+0.03}_{-0.03}$	8.68 ± 0.03	0.88
J152606.03+034530.7	−19.73	$0.80^{+0.03}_{-0.02}$	$0.02^{+0.04}_{-0.01}$	8.64 ± 0.01	0.78
J154933.50-004255.0	−19.45	$0.79^{+0.01}_{-0.02}$	$0.22^{+0.01}_{-0.01}$	8.68 ± 0.02	1.00
J154931.48-003406.1	−19.41	$0.89^{+0.02}_{-0.03}$	$0.47^{+0.02}_{-0.02}$	8.57 ± 0.03	1.38
J154925.24-003717.8	−16.62	$0.71^{+0.01}_{-0.01}$	$-0.04^{+0.01}_{-0.01}$	8.76 ± 0.01	0.02
J154914.49-004010.2	−20.49	$0.62^{+0.01}_{-0.01}$	$-0.29^{+0.02}_{-0.03}$	8.83 ± 0.02	1.57
J154925.12-003645.4	−20.70	$0.58^{+0.01}_{-0.01}$	$-0.28^{+0.02}_{-0.02}$	8.87 ± 0.01	1.16
J222013.98-074355.8	−21.21	$0.33^{+0.02}_{-0.03}$	$-0.44^{+0.07}_{-0.09}$	9.01 ± 0.05	0.69
J222014.86-073333.7	−21.31	$0.58^{+0.02}_{-0.03}$	$-0.30^{+0.07}_{-0.09}$	8.87 ± 0.06	2.62
J221934.90-073825.9	−20.85	$0.89^{+0.01}_{-0.01}$	$0.65^{+0.04}_{-0.05}$	8.59 ± 0.02	0.83
J221941.85-074703.8	−19.77	$0.65^{+0.01}_{-0.01}$	$-0.45^{+0.05}_{-0.05}$	8.80 ± 0.04	0.22
J221939.28-074744.5	−21.06	$0.04^{+0.08}_{-0.09}$	$-0.26^{+0.19}_{-0.34}$	9.11 ± 0.13	0.25
J221941.90-074825.7	−20.39	$0.74^{+0.01}_{-0.01}$	$-0.12^{+0.02}_{-0.01}$	8.71 ± 0.01	1.13

Notes. Column (2): absolute *B*-band magnitude from SDSS DR7 derived adopting the measured redshift. Column (3): metallicity-sensitive R_{23} parameter. Column (4): ionization-sensitive O_{32} parameter. Column (5): Gas-phase oxygen abundance. Column (6): star formation rate as derived using the Hβ uncorrected for Hβ stellar absorption line.